Simulation of supersonic base flow: effect of computational grid and turbulence model

M Dharavath, P K Sinha, and **D Chakraborty***
Directorate of Computational Dynamics, Defence Research and Development Laboratory, Hyderabad, Andhra Pradesh, India

The manuscript was received on 23 April 2009 and was accepted after revision for publication on 9 October 2009.

DOI: 10.1243/09544100JAERO600

Abstract: The supersonic base flow of a blunted cone-cylinder rocket model in the presence of a central propulsive jet is investigated numerically by solving three-dimensional Reynolds averaged Navier–Stokes equations in an unstructured mesh using a commercial computational fluid dynamics software. The effect of the computational grid and the turbulence model in predicting the radial variation of base pressure has been brought out. Very fine grid ($y^+ \sim 2$) is required to correctly predict the base pressure. The renormalized group $k-\varepsilon$ turbulence model performs better compared to the k–ω turbulence model in predicting the base pressure. It was observed that the base flow characteristics in the lower and upper portions of the base are significantly different due to the influence of model support.

Keywords: supersonic base flow, recirculation, computational fluid dynamics

1 INTRODUCTION

The supersonic base flow past an axisymmetric body continues to be an active research problem for fundamental flow physics as well as for engineering applications. The role of unsteady vortex shedding and large coherent structures in the supersonic base flow is not well understood. Recently, the planar visualization in the experiments on the supersonic base flow [**1**–**3**] showed evidence of large coherent turbulent structures. The origin of these coherent structures and their impact on the mean flow are far from understood. In engineering applications, missiles, launch vehicles, and projectiles have the complex base flow problem throughout their flight regime. Massive separation at the base leads to a dramatic decrease of the base pressure, causing base drag. For the supersonic flight regime, this base drag constitutes a significant portion of the total vehicle drag [**4**]. During the ascent phase in the atmosphere, the satellite launch vehicle and missiles encounter base heating due to the interaction of free stream and a hot propulsive jet. The energy transfer from the rocket exhaust to the vehicle base causes a significant rise in the base temperature. Hence, accurate prediction of base flow parameters is very important for the overall mission as well as for thermo-structural design of the vehicle base.

Schematic representation of the base flow with and without a propulsive jet is shown in Figs 1(a) and (b), respectively. The incoming flow separates at the base shoulder and a shear layer develops. For the jet off case, since the flow has to align with the centre-line, a recompression shock appears and the flow experiences an adverse pressure gradient. The streamlines that do not have sufficient energy to overcome the higher pressure turn back towards the base. The flow features with the jet on condition are also similar but the flow has to align with the jet axis. The interaction of the nozzle boundary layer and the shear layer in the base causes complex recirculation flow, which may not be symmetrical at the top and the bottom and depends on the pressure ratio of the jet and the free stream flow.

Because of the complex flow physics and engineering applications, base flow problems have been investigated extensively in the literature. Starting from the semi-empirical formulation of Chapman [**5**], a large number of research papers have appeared on supersonic base flow using experimental methods [**1**–**3**, **6**–**8**] and numerical methods [**9**–**19**] including Reynolds averaged Navier–Stokes (RANS) [**9**–**13**], detached eddy simulation (DES) [**14**], large eddy simulation (LES) [**15**–**17**], and direct numerical simulation

*Corresponding author: *Directorate of Computational Dynamics, Defence Research and Development Laboratory, P.O. Kanchanbagh, Hyderabad, Andhra Pradesh 500058, India.*
email: debasis_cfd@drdl.drdo.in; debasis_drdl@yahoo.co.in

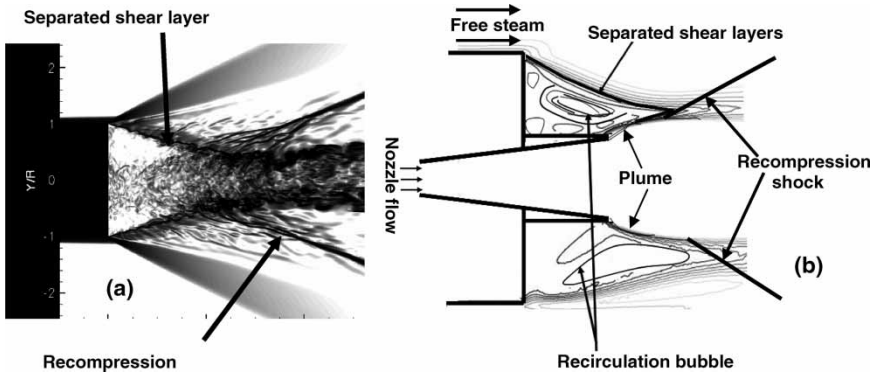

Fig. 1 Schematic of base flow problem: (a) without a propulsive jet and (b) with a propulsive jet

(DNS) [**18**, **19**]. Simon *et al.* [**16**] reviewed various RANS and LES methods applied to the supersonic base flow. Most of the numerical methods deal with base flow without the presence of a nozzle exhaust plume. In engineering application, RANS remains the most popular approach to solve the base flow, since semi-empirical procedures [**5**] cannot predict the variation of the base flow parameters and give only one average value in the base region. Sahu [**9**] simulated the experimental condition of Herrin and Dutton [**6**] and predicted the radial variation of base pressure. This study reveals that the predicted base pressure with the k–ε turbulence model is closer to the experimental value in comparison with other algebraic turbulence models. Chakraborty *et al.* [**10**] simulated the axisymmetric base flow experiment of Reid and Hastings [**20**] for different pressure ratios of free stream and propulsion jets. A grid adaptive Cartesian mesh-based Navier–Stokes solver AS3D [**21**] with the $k-\varepsilon$ turbulence model was used, and a qualitative match of computational base pressures with experimental values was obtained.

Most of the experimental methods use support sting from the rear of the test model. The presence of the support sting destroys the structure of the base flow on one side and makes the flow field fully three-dimensional (3D). Although a few empirical models were proposed to account the effect of sting, their reliability is yet to be established. Hence, it was suggested to combine the computational approach with experimental techniques to establish the reliability of the experiment. Research on 3D simulation of base flow in the presence of a propulsive jet and a support sting is very limited in the open literature. Bakker *et al.* [**22**] simulated the experimental condition of Bannink *et al.* [**8**]. Two sets of numerical simulations, namely:

(a) axisymmetric calculation without a support sting using a multi-dimensional upwind method [**23**];
(b) 3D simulation with a coarse grid using the finite-volume flux-difference (LORE) method [**24**] were performed to calculate the base flow with a propulsive jet and a support sting.

Four different turbulence models, namely the Spalart Allmaras (SA), k–ω, BSL (blending of k–ε and k–ω), and two-equation shear stress turbulence models, were compared for their ability to predict the base pressure. It was observed that:

(a) the two-equation model could give a reasonable qualitative description of the flow field, while the SA model could not predict the flow features properly;
(b) 3D simulations are required to find the effect of the support sting;
(c) 3D calculation did not adequately capture the flow features, as observed experimentally.

Hence, it is clear that the supersonic base flow in the presence of a propulsive jet and a support sting needs to be analysed in greater detail and the role of various turbulence models and computational grids needs to be studied for an accurate prediction of the base pressure.

In this work, the experimental condition of the supersonic base flow experiment conducted at University of Delft, the Netherlands, by Bannink *et al.* [**8**] was simulated numerically by solving 3D RANS equations in an unstructured mesh using commercial software [**25**]. The capability of two different turbulence models, namely the k–ω [**26**] and renormalized group (RNG)-based $k-\varepsilon$ [**27**] models, in predicting the base flow features in the presence of a propulsive jet and a support sting is presented, and the radial variation of base pressure is compared with the experimental results.

2 EXPERIMENTAL CONDITION FOR WHICH THE SIMULATIONS ARE CARRIED OUT

The axisymmetric blunted cone cylinder with the free base was tested [**8**] at zero incidence in the uniform supersonic stream in a transonic/supersonic wind tunnel TST 27 (270 mm $\times$ 280 mm test section) of the

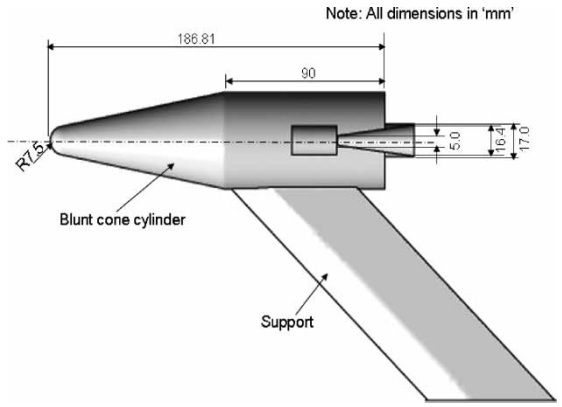

Fig. 2 The geometry of the test model

Aerospace Engineering Department of the Delft University of Technology. The sketch of the model is presented in Fig. 2. The length, semi-apex angle, and nose radius of the blunted cone forebody are 96.81 mm, 11°, and 7.5 mm, respectively, and are followed by a cylindrical afterbody of 90 mm length. From the centre of the base, a nozzle (its outer shape is circular cylinder) protrudes from which a high-pressure cold air jet is blown. The inner nozzle is conical with a divergence of 15°. The inner exit diameter of the nozzle is 16.4 mm and the diameter of the model base is 49.2 mm. The model is supported at the lower side of the aft part as shown in the figure. The support has a bevel angle of 30° and a thickness of 12 mm. The trailing edge of the support is truncated. The distance between the leading edge and the trailing edge is 50 mm and the support is attached to the model at 45°. Tests were performed at free stream Mach numbers of 1.96 and 2.98 and at stagnation pressures of 2.06 and 5.75 bar, respectively, with an accuracy of 1 per cent. The stagnation temperature was 285 ± 2 K. The central jet stagnation pressure ranged from 3.5 to 100 bar with an accuracy of 1.5 per cent. The Mach number at the nozzle exit was measured to be 3.96 ± 0.02. The Reynolds number based on the model length was 5.1×10^6 and 8.7×10^6 at free stream Mach numbers of 1.96 and 2.98, respectively. Ten pressure taps were provided in the cylindrical forebody of the model and 17 other pressure taps were used in the base to measure the radial and circumferential variations of base pressure.

3 COMPUTATIONAL METHODOLOGY

CFX-10 [**25**] is an integrated software system capable of solving diverse and complex multi-dimensional fluid flow problems. The software solves 3D RANS equations in a fully implicit manner. It is a finite volume method and is based on a finite-element approach to represent the geometry. The method retains much of the geometric flexibility of finite-element methods as well as the important conservation properties of the finite volume method. The software has four major modules:

(a) CFX build – imports CAD geometry or creates geometry and generates unstructured volume meshing based on the user input;
(b) preprocessor – sets up the boundary condition and the initial field condition;
(c) solver manager – solves the flow field based on the grid and the boundary condition;
(d) postprocessor – visualizes and extracts the results.

It utilizes numerical upwind schemes to ensure global convergence of mass, momentum, energy, and species. In the present study, the discretization of the convective terms is done by the second-order upwind difference scheme. Local time stepping has been used to obtain steady-state solutions. Two different turbulence models, namely the k–ω [**26**] and RNG-based k–ε turbulence models [**27**], are used. In the RNG k–ε model, the dissipation rate transport equation models the rate of strain rate that may be important for the treatment of non-equilibrium flows and flows in a rapid distortion limit such as massively separating flow and stagnation flow. The computational methodology has been validated extensively by comparing the experimental results on supersonic flow past a backward facing step with and without transverse injection [**28**, **29**]. The details of governing equations, turbulence models, and the discretization schemes are given in the following subsections.

3.1 Governing equations

The appropriate system of equations governing the turbulent compressible gas may be written as

Continuity equation

$$\frac{\partial \rho}{\partial t} + \frac{\partial}{\partial x_k}(\rho u_k) = 0, \quad k = 1, 2, 3$$

Momentum equation

$$\frac{\partial}{\partial t}(\rho u_i) + \frac{\partial}{\partial x_k}(\rho u_i u_k) + \frac{\partial p}{\partial x_i} = \frac{\partial(\tau_{ik})}{\partial x_i}, \quad i, k = 1, 2, 3$$

Energy equation

$$\frac{\partial}{\partial t}(\rho H) + \frac{\partial}{\partial x_k}(\rho u_k H) = -\frac{\partial}{\partial x_k}(u_j \tau_{jk}) + \frac{\partial q_k}{\partial x_k}$$
$$i, k = 1, 2, 3$$

where, ρ, u_i, p, and H are the density, velocity components, pressure, and total energy, respectively. Turbulent shear stress is defined as

$$\tau_{ik} = \mu \left(\frac{\partial u_i}{\partial x_k} + \frac{\partial u_k}{\partial x_i} \right)$$

$\mu = \mu_l + \mu_t$ is the total viscosity; μ_l and μ_t are the laminar and turbulent viscosities.

Laminar viscosity (μ_l) is calculated from the Sutherland law as

$$\mu_l = \mu_{ref}\left(\frac{T}{T_{ref}}\right)^{3/2}\left(\frac{T_{ref}+S}{T+S}\right)$$

where T is the temperature and μ_{ref}, T_{ref}, and S are known coefficients.

In eddy viscosity models, the stress tensor is expressed as a function of turbulent viscosity (μ_t). Based on dimensional analysis, a few variables (k, ε, ω) are defined as given below.

Turbulent kinetic energy k

$$k = \frac{\overline{u_i' u_i'}}{2}$$

Turbulent dissipation rate ε

$$\varepsilon \equiv \nu \overline{\frac{\partial u_i'}{\partial x_j}\left(\frac{\partial u_i'}{\partial x_j} + \frac{\partial u_j'}{\partial x_i}\right)}$$

Specific dissipation rate ω

$$\omega \sim \frac{\varepsilon}{k}$$

The turbulent viscosity μ_t is calculated as

$$\mu_t = c_\mu \frac{\rho k^2}{\varepsilon}$$

The heat flux q_k is calculated as $q_k = -\lambda(\partial T/\partial x_k)$, where λ is the thermal conductivity.

3.2 The k–ω turbulence model

The turbulent viscosity is calculated as a function of k and ω [**26**]

$$\mu_t = f\left(\frac{\rho k}{\omega}\right)$$

The turbulent kinetic energy (k) equation is

$$\frac{\partial}{\partial t}(\rho k) + \frac{\partial}{\partial x_i}(\rho k u_i) = \frac{\partial}{\partial x_j}\left(\Gamma_k \frac{\partial k}{\partial x_j}\right) + G_k - Y_k$$

The specific dissipation rate (ω) equation is

$$\frac{\partial}{\partial t}(\rho \omega) + \frac{\partial}{\partial x_i}(\rho \omega u_i) = \frac{\partial}{\partial x_j}\left(\Gamma_\omega \frac{\partial \omega}{\partial x_j}\right) + G_\omega - Y_\omega$$

where G_k, Y_k, Γ_k and G_ω, Y_ω, Γ_ω are the production, dissipation, and diffusion terms of the k and ω equations, respectively.

3.3 The RNG k–ε model

An improved method for rapidly strained flows based on a rigorous statistical technique [**27**] is also used in the present calculations. The k and ε equations are given below

$$\frac{\partial}{\partial t}(\rho k) + \frac{\partial}{\partial x_i}(\rho k u_i) = \frac{\partial}{\partial x_j}\left(\alpha_k \mu_{eff} \frac{\partial k}{\partial x_j}\right) + G_k - \rho\varepsilon - Y_M$$

$$\frac{\partial}{\partial t}(\rho \varepsilon) + \frac{\partial}{\partial x_i}(\rho \varepsilon u_i) = \frac{\partial}{\partial x_j}\left(\alpha_\varepsilon \mu_{eff} \frac{\partial \varepsilon}{\partial x_j}\right) + C_{1\varepsilon} \times \frac{\varepsilon}{k} \times G_k - C_{2\varepsilon}\rho\frac{\varepsilon^2}{k} - R_\varepsilon$$

where G_k is the generation of turbulence kinetic energy due to the mean velocity gradients, calculated as $G_k = -\rho\overline{u_i' u_j'}(\partial u_j/\partial x_i)$, and Y_M represents compressibility effects given by $Y_M = 2\rho\varepsilon M_t^2$. The turbulent Mach number M_t is given by $M_t = \sqrt{k/a^2}$.

The model constants are taken as $C_{1\varepsilon} = 1.42$, $C_{2\varepsilon} = 1.68$, $C_\mu = 0.0845$, σ_k and $\sigma_\varepsilon = 1.393$.

The additional term in the ε equation R_ε is given as $R_\varepsilon = [C_\mu \rho \eta^3(1 - \eta/\eta_0)]/(1 + \beta\eta^3)(\varepsilon^2/k)$, where $\eta \equiv Sk/\varepsilon$, $\eta_0 = 4.38$, and $\beta = 0.012$.

3.4 Discretization of governing equations

The CFX-10 solver utilizes a finite volume approach, in which the conservation equations in differential form are integrated over a control volume described around a node, to obtain an integral equation. The pressure integral terms in the momentum integral equation and the spatial derivative terms in the integral equations are evaluated using the finite-element approach. An element is described with eight neighbouring nodes. The advective term is evaluated using upwind differencing with physical advection correction. The set of discretized equations form a set of algebraic equations: $A\boldsymbol{x} = b$, where $\boldsymbol{x}$ is the solution vector. The solver uses an iterative procedure to update an approximated x_n (the solution of x at the nth time level) by solving for an approximate correction x' from the equation $A\boldsymbol{x}' = \boldsymbol{R}$, where $\boldsymbol{R} = \boldsymbol{b} - A\boldsymbol{x}_n$ is the residual at the nth time level. The equation $A\boldsymbol{x}' = \boldsymbol{R}$ is solved approximately using an approach called the incomplete lower–upper factorization method.

4 RESULTS AND DISCUSSIONS

The computational domain and the typical grid structure are shown in Fig. 3. The inflow plane is taken at 45 mm ahead of the blunt cone, while the outflow plane is taken at 230 mm behind the base. Three different unstructured grids of size 0.5, 1.9, and 3.4 million

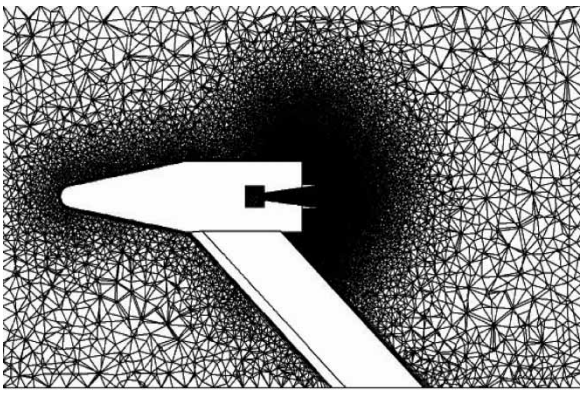

Fig. 3 Computational grid around the model

were generated in the domain using CFX – build and ICEM – computational fluid dynamics (CFD) grid generator. The grids are made progressively finer from the coarse mesh of 0.5 million to 3.4 million by refining the grid in the base region and the separated shear layer region to capture the complex nature of the base flow. (The effect of the grid on the flow feature will be shown later in the section.) The minimum grid spacing near the base region is about 0.1 mm, which corresponds to $y^+(= yu_\tau\rho/\mu) \sim 2$. In the computation, the X-axis is taken along the longitudinal direction, while the Y- and Z-axes are taken along the height and the width of the model. The origin is taken at the centre of the blunt cone. Although the experiment is conducted for two free stream Mach numbers, the present simulation considers the case of Mach 2.98 only. The free stream and central jet properties used in the simulation are tabulated in Table 1.

The cold air has been considered for the central jet with a stagnation pressure and a temperature of 31.3 bar and 287 K, respectively. The nozzle exit Mach number is 3.96. The stagnation pressure, stagnation temperature, and Mach number of the free stream flow are 5.75 bar, 287 K, and 2.98, respectively. As the free stream at the inflow is supersonic, the free stream velocity, pressure, and temperature are set in the inflow plane and the supersonic outflow conditions are set for the outflow plane. The nozzle inlet plane is placed in the convergent portion of the nozzle, and the subsonic boundary conditions of constant total pressure and total temperature of the jet have been prescribed. A log normalized rms value of 10^{-5} has been set for the convergence criteria.

Table 1 Inflow condition for the free stream and the central jet

Parameter	Free stream condition	Central jet
Stagnation pressure (bar)	5.75	31.3
Stagnation temperature (K)	287	287
Mach number	2.98	3.96 (at nozzle exit)

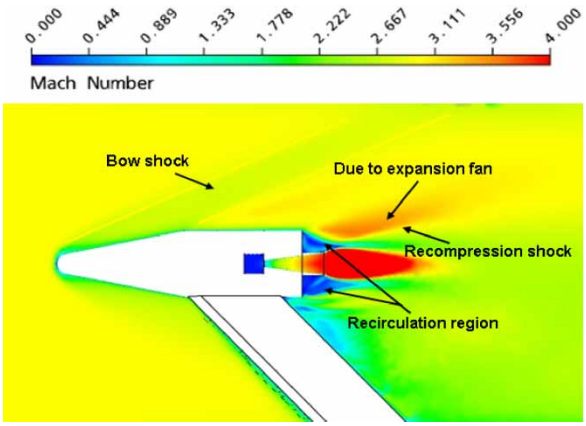

Fig. 4 Mach number contour in the plane of symmetry

The Mach number contour on the plane of symmetry is shown in Fig. 4 to depict the qualitative features of the flow. The bow shock from the blunt cone, expansion from the base shoulder, central jet, recirculation region in the base region, and recompression shock are clearly seen from the figure. Owing to the effect of the support sting, the recirculation patterns in the upper and lower portions in the base region are different. To show the nozzle plume jet structure, pressure distribution in the plane of symmetry is presented in Fig. 5. The shock structure including the first shock cell is crisply captured in the simulation. The area ratio and the total pressure of the central propulsive nozzle are 10.75 and 31.3 bar, respectively. For the ideally expanded case, the calculated exit Mach number is 3.98 and the static pressure at the nozzle exit (p_e) is 0.217 bar. If the free stream static pressure (p_∞) of 0.1613 bar is considered, the pressure ratio (p_e/p_∞) will be 1.35. For the present case, the exact pressure ratio will not be 1.35 as the ambient pressure near the nozzle exit is much lower than free stream pressure. A better estimate of the pressure ratio will be p_e/p_{bavg}, where p_{bavg} is the average base pressure in the vicinity of the nozzle exit. The average base pressure is calculated from the simulated results and the value of p_{bavg} is 0.03 bar, which gives a pressure ratio of 7.3, which is much larger than 1.35

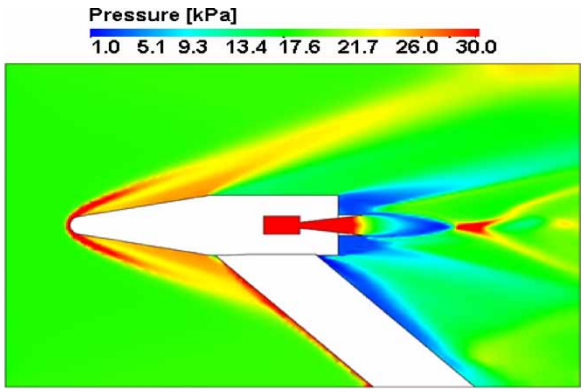

Fig. 5 Pressure contour in the plane of symmetry

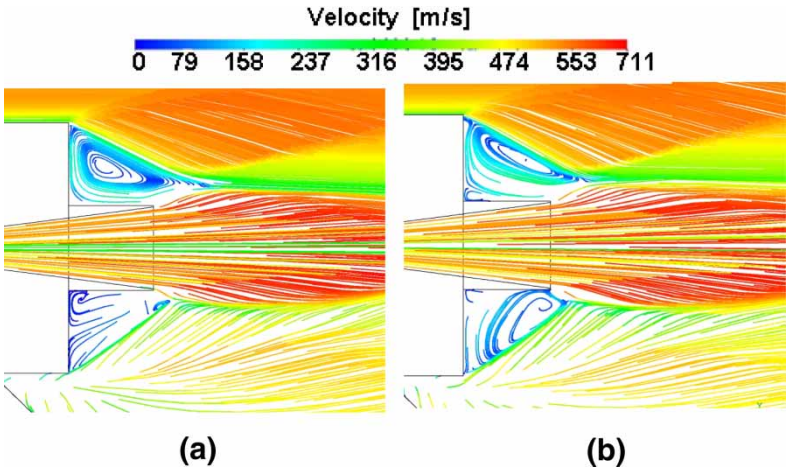

Fig. 6 Streamline contour at the base region recirculation zone

(pressure ratio corresponding to free stream pressure). For this underexpansion, one shock cell of length 6.6r (r being the nozzle radius) is observed.

To illustrate the effect of model support clearly, the flow field in the base region is zoomed and streamlines contours (coloured with velocity) are presented for both the RNG k–ε and k–ω turbulence models in Fig. 6. Recirculation patterns in the upper and lower portions of the base region are different. Although one big and two small separation bubbles are seen in both the upper and lower portions of the base region, the shapes and sizes of the separation bubble differ considerably. The core of the major separation bubble in the upper portion is towards the free stream but the core of the separation bubble in the lower part is towards the nozzle wall. The separating shear layers in the upper and lower portions of the body differ in shape because of the model support. The recirculating flow in the lower portion of the base (wake of the model support) is more organized for the k–ω turbulence model compared to the RNG k–ε turbulence model. The eddy viscosity distribution in the base region is compared between the two turbulence models in Fig. 7. Eddy viscosity distributions between the two models are different in the base region. The RNG k–ε model predicts a higher eddy viscosity in the upper portion of the base, while the k–ω model predicts a higher value in the lower portion of the base.

The axial distribution of the surface pressure in the cylindrical part of the model is compared between experiment and computation for the k–ω and RNG k–ε turbulence models and two grids, namely 0.19 and 0.34 million in Fig. 8. Very good agreement between the experiment and the computation is observed. This demonstrates that the results in the forebody are grid independent and both the turbulence models are predicting the surface pressure in the forebody quiet accurately. Proper prediction of the radial variation of the base pressure is very challenging for the CFD tools. Various authors [**7**, **22**, **30**] reported the difficulties in

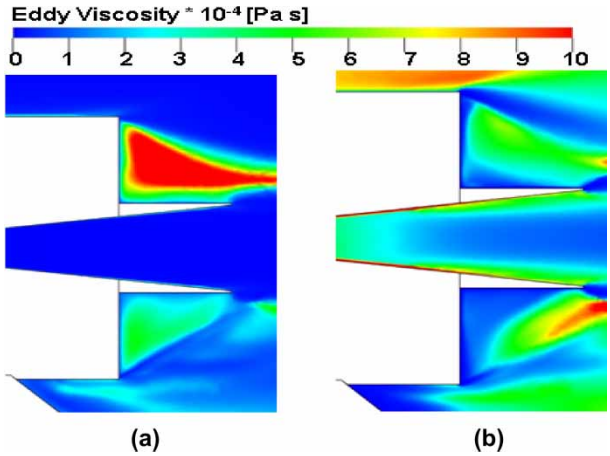

Fig. 7 Eddy viscosity distribution in the plane of symmetry

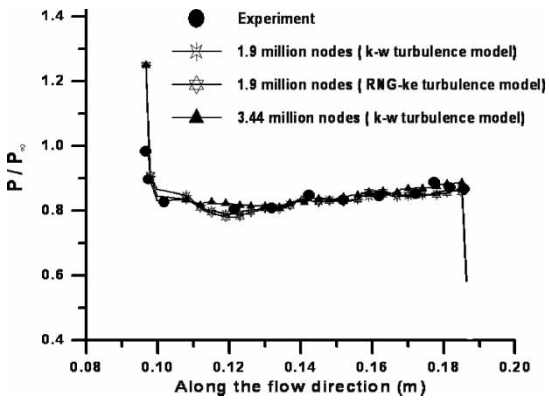

Fig. 8 Comparison of axial distribution of surface pressure

quantitative prediction of the radial variation of base pressure and suggested further development of CFD tools. Radial variation of the base pressure obtained with the k–ω turbulence model with different grids is compared with the experimental result in Fig. 9.

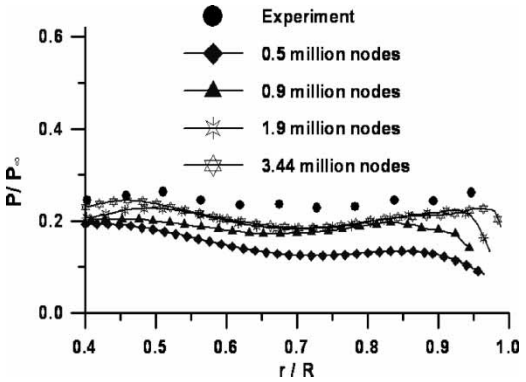

Fig. 9 Radial base pressure comparison with the k–ω turbulence model for different grids

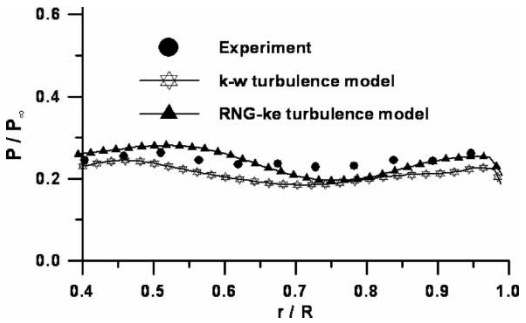

Fig. 10 Radial base pressure comparison with the k–ω and RNG k–ε turbulence models

Although an increase in the grid size has improved the prediction, yet there is about 20 per cent maximum difference between the experimental and computational values. The radial variations of the base pressure predicted with the k–ω and RNG K–ε models are compared with experimental results in Fig. 10 for the finest grid of 3.44 million. The overall comparisons are very good. The RNG k–ε model predicts the radial variation of the base pressure better than the k–ω model. The extra strain rate term included in the dissipation rate transport equation of the RNG K–ε model may be responsible for the better prediction of massively separated flow. To quantify the effect of the model support on the base pressure, radial variation of static pressure in the lower and upper portions of the base is presented in Fig. 11. The lower portion of the base experiences lesser base pressure compared to the upper portion because of the presence of a support sting. Also, radial variation of base pressure in the lower portion is less compared to the radial variation of base pressure in the upper portion. The maximum difference in base pressure between the lower portion and the upper portion is about 50 per cent. As explained earlier, the central jet is underexpanded (pressure ratio $p_e/p_{bavg} = 7.25$). The shock cell pressure profiles in the exhaust plume jet axis at various axial stations at the nozzle exit and at a distance of r, $2r$, and $3r$ are presented in Fig. 12. It is clear

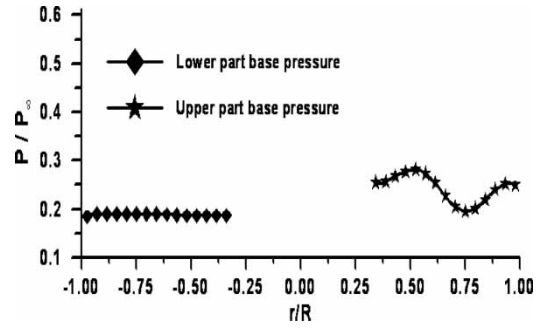

Fig. 11 Radial variation of the base in lower and upper portions of the base

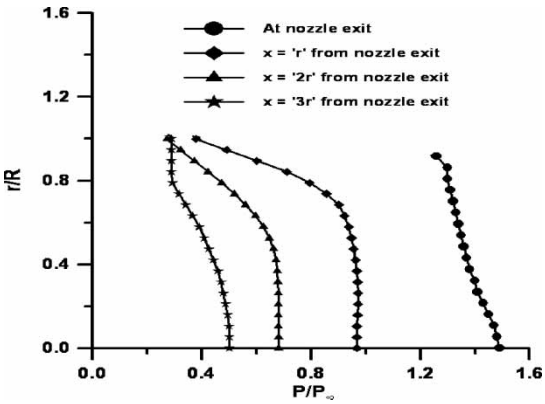

Fig. 12 Radial variation of base pressure at various axial stations in the exhaust plume

from the figure that the plume is still under expansion and the pressure is decreasing as one proceeds downstream. The shock structure in the shear layer outside the plume region is not affecting the flow field in the plume significantly.

5 CONCLUDING REMARKS

Supersonic base flow has been investigated by solving the 3D Navier–Stokes equation in an unstructured grid using a commercial CFD software. Two different turbulence models, namely the k–ω and RNG k–ε models, have been employed to determine their predictive capability of the base pressure. Although both the models performed well in predicting the forebody surface pressure, the RNG-based k–ε model performed better in predicting the radial variation of base pressure. It has been found that very fine meshing ($y^+ \sim 2$) is required to predict the base pressure accurately. The wake caused by the support of the model is seen to affect the flow pattern in the lower portion of the base.

REFERENCES

1 **Bourdon, C. J.** and **Dutton, J. C.** Planar visualizations of large-scale turbulent structures in axisymmetric supersonic separated flows. *Phys. Fluids,* 1999, **11**(1), 201–213.

2 **Bourdon, C. J., Dutton, J. C., Smith, K. M.,** and **Mathur, T.** Planar visualizations of large-scale turbulent structures in axisymmetric supersonic base flow. AIAA paper 98-0624, 1998.

3 **Bourdon, C. J.** and **Dutton, J. C.** Visualizations and measurements of axisymmetric base flows altered by surface disturbances. AIAA paper 2001-0286, 2001.

4 **Rollstin, L.** Measurement of inflight base-pressure on artillery fired projectile. AIAA paper 87-2427, 1987.

5 **Chapman, D. R.** An analysis of base pressure at supersonic velocities and comparison with experiments. NACA report 1051, 1951.

6 **Herrin, J. L.** and **Dutton, J. C.** Supersonic base flow experiments in the near wake of a cylindrical afterbody. *AIAA J.,* 1994, **32**(1), 77–83.

7 **Joel, P. K.** and **Dutton, J. C.** Acetone PLIF imaging of a supersonic axisymmetric base flow with mass bleed. AIAA paper 2004-2650, 2004.

8 **Bannink, W. J., Baker, P. G.,** and **Houtman, E. M.** FESTIP aerothermodynamics: experimental investigation of base flow and exhaust plume interaction. Memorandum M-775, Aerospace Engineering, Delft University of Technology, 1997.

9 **Sahu, J.** Numerical computation of supersonic base flow with special emphasis on turbulence modeling. *AIAA J.*, 1994, **32**(7), 1547–1549.

10 **Chakraborty, D., Kumar, P., Balu, R.,** and **Adimurthy, V.** Numerical simulation of axisymmetric base flow in the presence of propulsive jet. *J. Aeronaut. Soc. India*, 2001, **53**, 35–38.

11 **Benay, R.** and **Servel, P.** Two-equation k–σ turbulence model: application to a supersonic base flow. *AIAA J.*, 2001, **39**(3), 407–416.

12 **Chuang, C. C.** and **Chieng, C. C.** Supersonic base-flow computation using higher-order closure turbulence models. *J. Spacecr. Rockets,* 1996, **33**(3), 374–380.

13 **Papp, J. L.** and **Ghia, K. N.** Application of the RNG turbulence model to the simulation of axisymmetric supersonic separated base flows. AIAA paper 2001-0727, 2001.

14 **Forsythe, J. R., Hoffmann, K. A., Cummings, R. M.,** and **Squires, K. D.** Detached-eddy simulation with compressibility corrections applied to a supersonic axisymmetric base flow. *J. Fluids Eng.,* 2002, **124**, 911–923.

15 **Soshi, K.** and **Fujii, K.** Computational study of a supersonic base flow using LES/RANS hybrid methodology (RANS/LES). AIAA paper 2004-68, 2004.

16 **Simon, F., Deck, S., Guillen., P.,** and **Sagant, P.** Reynold-averaged Navier–Stokes/large eddy simulation of supersonic base flow. *AIAA J.*, 2006, **44**(11), 2578–2590.

17 **Fureby, C., Nilsson, Y.,** and **Andersson, K.** Large-eddy simulation of supersonic base flow. AIAA paper 99-0426, 1999.

18 **Sandberg, R. D.** and **Fasely, H. F.** Instability mechanisms in supersonic base flows. AIAA paper 2004-593, 2004.

19 **Sandberg, R. D.** and **Fasely, H. F.** Numerical simulation of supersonic base flows. AIAA paper 2005-98, 2005.

20 **Reid, J.** and **Hastings, R. C.** The effect of a central jet on the base pressure of a cylindrical after-body in a supersonic stream. Aeronautical Research Council (Great Britain) Reports and Memoranda No. 3224, December 1959.

21 *Aeroshape 3D – technique and general description* (Computational Aerodynamics System Co., Moscow).

22 **Bakker, P. G., Bannink, W. J., Servel, P.,** and **Reijasse, P.** CFD validation for base flows with and without plume interaction. AIAA paper 2002-0438, 2002.

23 **Houtman, E. M., Weide, V. D., Deconinck, E.,** and **Bakker, P. G.** Computational analysis of base flow/jet plume interaction. In Proceedings of the Third European Symposium on Aerothermodynamics for Space Vehicles, ESA SP – 426, 1998, pp. 605–612.

24 **Walpot, L. M. G. F.** *Development and application of a hypersonic flow solver*. PhD Thesis, Aerospace Engineering Department, Delft University of Technology, The Netherlands, 2002.

25 Ansys. *User manual, CFX-10*, 2006 (Ansys).

26 **Wilcox, D. C.** Multiscale model for turbulent flows. *AIAA J.*, 1988, **26**(11), 1311–1320.

27 **Yakhot, V.** and **Orszag, S. A.** Renormalization group analysis of turbulence. *J. Sci. Comput.*, 1986, **1**, 3–51.

28 **Manna, P.** and **Chakraborty, D.** Numerical investigation of transverse sonic injection in a nonreacting supersonic combustor. *Proc. IMechE, Part G: J. Aerospace Engineering*, 2005, **219**(3), 205–215. DOI: 10.1243/095441005X30261.

29 **Manna, P.** and **Chakraborty, D.** Numerical investigation of confinement effect on supersonic turbulent flow past backward facing step with and without transverse injection. *J. Aerosp. Sci. Technol.*, 2009, **61**(2), 283–294.

30 **Chutkey, K., Vasudevan, B.,** and **Balakrishnan, N.** Flowfield analysis of truncated and clustered linear plug nozzle. In Proceedings of the IISc Centenary International Conference and Exhibition on Aerospace Engineering, May 2009, pp. 243–252.

APPENDIX

Notation

A	coefficient matrix
G_k, G_ω, G_ε	production terms for k, ω, and ε
H	enthalpy
k	turbulent kinetic energy
L	length of the combustor
M	Mach number
p	pressure
Pr	Prandtl number
Q	heat flux
r	nozzle radius
R	residue
R_ε	strain rate term in the ε equation of the RNG k–ε model
S	Sutherland constant
t	time

T	temperature
u	axial velocity
U	velocity in general
w	transverse velocity
W	width of the combustor
x	axis in general
X, Y, Z	coordinate axes
$Y_k, Y_\omega, Y_\varepsilon$	dissipation terms for k, ω, and ε
$\Gamma_k, \Gamma_\omega, \Gamma_\varepsilon$	diffusion terms for k, ω, and ε
ε	turbulent kinetic energy dissipation rate
λ	thermal conductivity
μ	dynamic viscosity
ρ	density
$\sigma_k, \sigma_\varepsilon$	coefficients for the k and ε equations
τ	shear stress

Subscripts

bavg	average base pressure
i, j, k	axial direction
l	laminar
ref	reference value
t	turbulent
∞	free stream